ORIGINAL PAPER

Electrochemistry of bismuth interlayers in $(Bi_2)_m(Bi_2Te_3)_n$ superlattice

Aliaksei Bakavets[1,2] · Yauhen Aniskevich[1,2] · Genady Ragoisha[1] · Alexander Mazanik[3] · Natalia Tsyntsaru[4,5] · Henrikas Cesiulis[4] · Eugene Streltsov[2]

Abstract

Selective electrochemical transformations of bismuth interlayers in $(Bi_2)_m(Bi_2Te_3)_n$ superlattices can be of interest as a means of thermoelectric materials design based on bismuth telluride. In this work, the interlayers in the electrodeposited $(Bi_2)_m(Bi_2Te_3)_n$ superlattice structures formed by pulse potential controlled electrodeposition were characterized with electrochemical microgravimetry on quartz crystal electrodes, cyclic voltammetry, potentiodynamic electrochemical impedance spectroscopy (PDEIS), and in situ Raman spectroscopy. The oxidation potential of bismuth in the interlayers is in between the potentials of metallic bismuth and bismuth telluride anodic oxidation, which allows electrochemical detection and selective anodic dissolution of the interlayer bismuth. Microgravimetry and cyclic voltammetry have provided monitoring of bismuth interlayer dissolution and the subsequent underpotential deposition (upd) of bismuth adatoms onto Bi_2Te_3 layers in the electrochemically created slits. PDEIS provided separate monitoring of the interfacial charge transfer, spatially restricted diffusion, capacitance of faradaic origin, and double-layer capacitance, which disclosed different variations of the electrochemical interface area in the superlattices with initial bismuth content below and above that of Bi_4Te_3. In situ Raman spectroscopy has monitored the removal of bismuth interlayers and distinguished different locations of Bi adatoms in two stages of Bi upd. The electrochemically created slits of molecular dimension have a potential of being used as sieves, e.g., to provide selective accessibility of the electrochemically created centers inside them to molecules and ions in multi-component solutions.

Keywords Bismuth telluride · Bismuth interlayer · Superlattice · Impedance spectroscopy · Quartz crystal microbalance · Raman spectroscopy

Introduction

$(Bi_2)_m(Bi_2Te_3)_n$ superlattices formed by alternation of elementary five-atomic layer fragments of Bi_2Te_3 crystal structure (Bi_2Te_3 quintuples) and bismuth biatomic layers

Dedicated to Professor György Inzelt on the occasion of his 75th birthday with recognition of his valuable contribution to electrochemistry.

✉ Genady Ragoisha
  ragoisha@yahoo.com

1   Research Institute for Physical Chemical Problems, Belarusian State University, Minsk, Belarus

2   Faculty of Chemistry, Belarusian State University, Minsk, Belarus

3   Faculty of Physics, Belarusian State University, Minsk, Belarus

4   Faculty of Chemistry and Geosciences, Vilnius University, Vilnius, Lithuania

5   Institute of Applied Physics, Chisinau, Moldova

are of interest for thermoelectric material design, due to the opportunity of breaking the tradeoff between electric and thermal conductivities that normally limits figure of merit of individual bismuth telluride [1–3]. Much attention in electrochemistry of bismuth telluride has been given to electrodeposition of Bi_2Te_3 nanoparticles of various sizes and shapes [4–13], while $(Bi_2)_m(Bi_2Te_3)_n$, $(Bi_2)_m(Bi_2Se_3)_n$ [14–17] and $(Sb_2)_m(Sb_2Te_3)_n$ [18] superlattices were usually obtained by non-electrochemical methods. A superlattice extends unusual properties of nano object to macro dimensions, so that the heterogeneity on nanometer level affects both physical and electrochemical properties of large particles with internal superlattice structure.

We have recently [19] developed a pulsed electrodeposition technique with two potentiostatically controlled potentials — electrodeposition and refinement potentials for preparation of superlattice materials of $(Bi_2)_m(Bi_2Te_3)_n$ series with variable interlayer bismuth content. The formula $(Bi_2)_m(Bi_2Te_3)_n$ fits to different superlattices. With m increasing up to $m=n$, bismuth atomic bilayers are randomly

alternated with Bi_2Te_3 quintuples or stacks of few quintuples until each van der Waals plane of Bi_2Te_3 structure (a plane between tellurium atoms belonging to the neighboring quintuples) is filled by bismuth bilayer at Bi_4Te_3 net composition. The corresponding structure is shown in Fig. 1 on the left side. According to X-ray photoelectron spectroscopy, the interlayer bismuth is in Bi(0) oxidation state [19]. The opportunity of electrochemical formation of bismuth bilayers between Bi_2Te_3 during the electrosynthesis results from underpotential deposition of Bi adlayer on Bi_2Te_3 and stability of the structure that combines two adlayers in a bilayer, confirmed by density functional theory calculations [19].

At very high precursor Bi(III)/Te(IV) molar ratio in the electrolyte solution at $(Bi_2)_m(Bi_2Te_3)_n$ electrodeposition, the excessive bismuth cannot fit into bilayers, so thicker interlayers have to be formed at $m > n$, tending to double bilayers in Bi_2Te or even thicker interlayers at especially high Bi(III)/Te(IV). In this work, "low bismuth content" refers to $(Bi_2)_m(Bi_2Te_3)_n$

with $m \leq n$, contrary to "high bismuth content" which refers to $(Bi_2)_m(Bi_2Te_3)_n$ with bismuth content higher than in Bi_4Te_3. Bismuth interlayers of both kinds are easily distinguished from metallic bismuth by significantly higher anodic oxidation potential. But different interlayers are not easily discriminated by their potentials of anodic oxidation, as the anodic oxidation of bismuth in the interlayer is a non-stationary process which is strongly dependent on mass transport. Materials which contain metallic and interlayer bismuth give two distinct peaks of bismuth anodic oxidation with above 100 mV separation. Bi_2Te_3 framework of $(Bi_2)_m(Bi_2Te_3)_n$ superlattice oxidizes at higher potential, and this provides the opportunity of selective anodic oxidation of bismuth interlayers in $(Bi_2)_m(Bi_2Te_3)_n$ superlattice structures. The selective anodic oxidation and dissolution of bismuth from interlayers in the superlattices with low bismuth content is of special interest, as it was shown by XRD analysis to proceed with preservation of the original superlattice structure [19] (Fig. 1). The stability of the superlattice structure framework at the anodic treatment provides a way for the introduction of defects that control thermoelectric properties of $(Bi_2)_m(Bi_2Te_3)_n$ by affecting the tradeoff between thermal and electric conductivities. Also, the non-destructive oxidative dissolution of bismuth interlayers may provide a way for bismuth substitution by other elements in a design of more complex superlattice structures.

The goal of this work is the examination of anodic oxidation of bismuth interlayers in the electrodeposited $(Bi_2)_m(Bi_2Te_3)_n$ by four potentiodynamic methods: microgravimetry on quartz crystal electrodes, cyclic voltammetry (CV), potentiodynamic electrochemical impedance spectroscopy (PDEIS), and Raman spectroscopy applied in the potentiodynamic mode.

The use of potentiodynamic mode is essential, as the anodic dissolution of bismuth from bismuth interlayers is an inherently non-stationary process which makes applications of stationary versions of the same methods much less productive. Additionally to the anodic oxidation and dissolution of bismuth from the interlayers, we examined the reverse deposition of bismuth into the electrochemically created slits and found that a significant amount of bismuth can be reintroduced into the Bi_2Te_3 framework at the electrochemical condition of underpotential deposition, despite the anodic dissolution of the interlayers was a generally irreversible process.

Experimental

Electrodeposition and potentiodynamic voltammetry

The superlattice materials were synthesized by pulse potential–controlled electrodeposition [19, 29]. The electrolyte composition was typically 7.5 mmol L^{-1} of

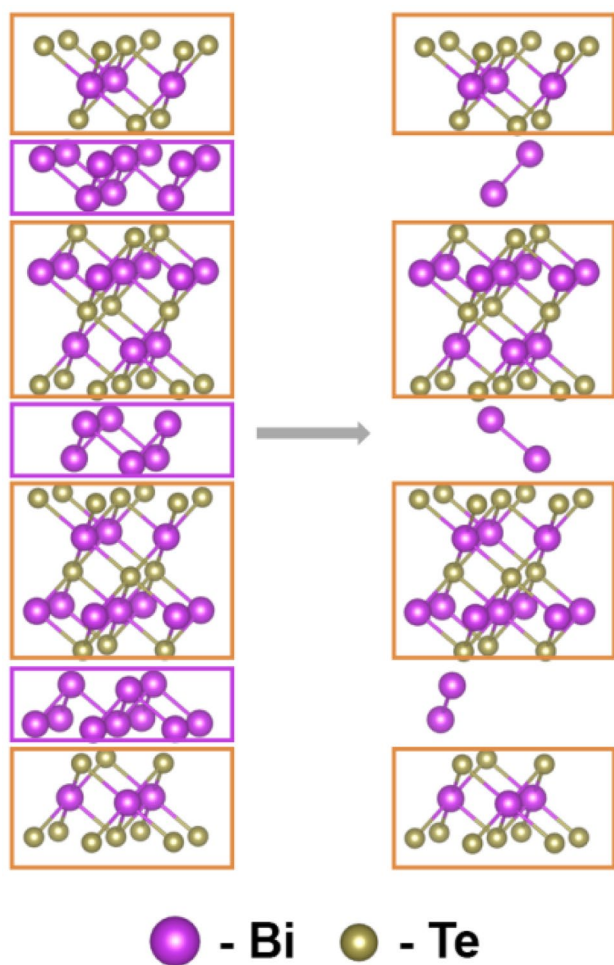**Fig. 1** Schematic presentation of the selective anodic dissolution of bismuth from interlayers in $(Bi_2)m(Bi_2Te_3)n$ superlattice with "low" bismuth content

⬤ - Bi ⬤ - Te

Bi(NO$_3$)$_3$, 2.5 mmol L^{-1} of TeO$_2$, and 1 mol L^{-1} of HNO$_3$ at electrodeposition of (Bi$_2$)$_m$(Bi$_2$Te$_3$)$_n$ superlattices with "low" bismuth content, i.e., below that corresponding to Bi$_4$Te$_3$ formula. While 8.75 mmol L^{-1} of Bi(NO$_3$)$_3$, 1.25 mmol L^{-1} of TeO$_2$ in 1 mol L^{-1} of HNO$_3$ electrolyte solution was used for electrodeposition of (Bi$_2$)$_m$(Bi$_2$Te$_3$)$_n$ superlattices with "high" bismuth content. Stainless steel substrates were polished with 0.05 μm alumina suspension after pretreatment in boiling concentrated nitric acid. The working part of the electrode was separated from the rest of the electrode with water-resistant varnish, and the electrode was subjected to ten potential cycles between −0.4 V and 0.8 V at 50 mV s^{-1} in 1 mol L^{-1} nitric acid before the electrodeposition which was carried out in a three-electrode cell with a working electrode, Ag|AgCl|KCl(3 M) reference, and Pt counter electrode. Effects of parameters of the electrodeposition on nucleation, film growth, and film morphology were presented earlier [19, 29]. The electrodeposited films were compact, polycrystalline, and firm sufficiently to be detached with epoxy resin from steel support for measurement of thermoelectric properties at 120 min deposition time, when the thickness reached 3 μm (not presented in this work). The pulse potential mode provided phase composition independence on film thickness. This allowed us to use thinner films for the electrochemical examination (approx. 1.5 μm in electrochemical microgravimetry, 1 μm in potentiodynamic Raman spectroscopy, and 0.5 μm in PDEIS) with confidence in their electrochemical property relevance to those of thicker films. The use of thin films in PDEIS favored avoiding complications in circuit analysis which could be otherwise affected by contribution to frequency response of charge transfer inside a thick film. The sum of the 0.5 μm film resistance with resistance of electrolyte solution, evaluated from PDEIS spectra, was much below 10 Ω cm^2. Geometric surface area of electrodes was 113 mm^2 in electrochemical microgravimetry, 25 mm^2 in potentiodynamic Raman spectroscopy, and 5 mm^2 in PDEIS experiments.

Gamry Series G300 potentiostat was used for potential control in electrodeposition, cyclic voltammetry (CV), and potentiodynamic microgravimetry. After the electrode activation at −0.4 V for 10 s, a square potential waveform was applied at 0.1 Hz and 5% duty cycle (0.5 s active electrodeposition at −100 mV with the subsequent switching to 20 mV for the rest time of each period) with a continuous stirring of the electrolyte solution.

Quartz crystal microbalance

Cyclic potentiodynamic microgravimetry was performed with QCM200 Quartz Crystal Microbalance (QCM) on Au-coated quartz crystals (Stanford Research Systems). The cell setup was the same as in potentiodynamic voltammetry.

Potentiodynamic electrochemical impedance spectroscopy

Potentiodynamic electrochemical impedance spectra were acquired with a home-built spectrometer [20, 21] and analyzed with built-in PDEIS software described in [22]. The software for analysis of PDEIS data extends the algorithms of ordinary impedance spectra analysis, which were applied in EIS Spectrum Analyser [23], to the analysis of impedance spectra dependences on variable potential. The resulting potentiodynamic profiles of equivalent circuit parameters present contributions of the corresponding circuit elements to the potentiodynamic electrochemical response in a way similar to that of mass and current profiles in the potentiodynamic microgravimetry. The potentiodynamic frequency response was acquired in 22 frequencies in the interval between 10 and 440 Hz. Relatively thin films of (Bi$_2$)$_m$(Bi$_2$Te$_3$)$_n$ pulse deposited at 15 min were used to avoid complications of the frequency response by interparticle electron transfer within the film.

Raman spectroscopy

Raman spectra were acquired at room temperature using a Nanofinder HE confocal spectrometer (LOTIS TII, Belarus-Japan) with a 532-nm solid-state CW laser as the excitation source. Incident optical power was 2 mW. The Raman signal was obtained from the part of the electrode surface illuminated by focused laser beam. Due to strong absorbance of the electrode material at the excitation wavelength, the signal characterized predominantly the electrochemically stimulated changes in a thin layer close to the electrochemical interface. Metrohm Autolab was used to control the potential in the potentiodynamic mode. CV and Raman data were collected in the potentiodynamic mode at 1 mV s^{-1} in a three-electrode cell with Au counter and Bi reference electrodes in 10 mmol L^{-1} of Bi(NO$_3$)$_3$, and 1 mol L^{-1} of HNO$_3$ electrolyte. Bi/Bi^{3+} reference electrode was used to comply with a confinement of the experiment working space. All other potentials in this work are presented with reference to Ag|AgCl|KCl(3 M) electrode.

Results and discussion

Potentiodynamic microgravimetry

Observation of the selective anodic oxidation and dissolution of bismuth interlayers from (Bi$_2$)$_m$(Bi$_2$Te$_3$)$_n$ superlattice requires the use of strongly acidic medium to prevent suppression of the reaction product evacuation by Bi(III) hydrolysis. Figure 2 shows the effect of the electrolyte composition on the anodic

Fig. 2 Linear sweep voltammograms showing effect of electrolyte composition on the selective anodic oxidation of bismuth interlayers in the electrodeposited $(Bi_2)m(Bi_2Te_3)_n$ superlattices at high bismuth content. $dE/dt = 1$ mV s^{-1}
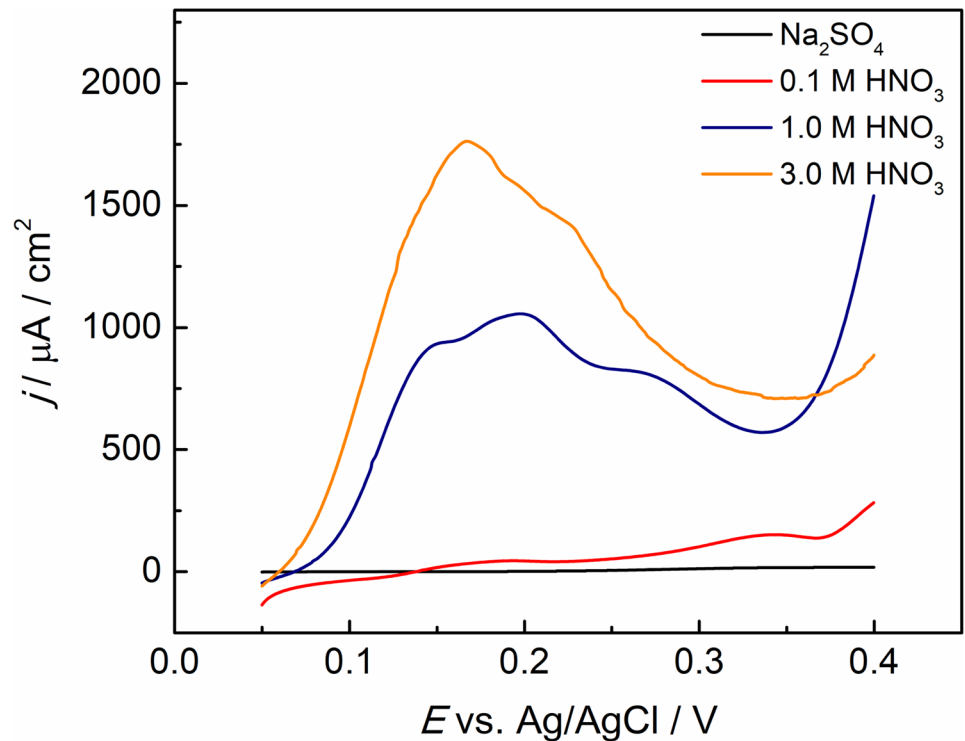

current in the potential range of bismuth interlayer anodic oxidation. 1 M HNO$_3$ was the optimal composition which provided both the efficient evacuation of Bi(III) and sufficient stability of the remaining bismuth telluride framework. Electrode mass change monitoring with QCM has proved to be helpful for understanding the electrochemistry of systems with the charge transfer accompanied by mass transport [24–27].

Figure 3a, b show variation of mass and current in a cyclic potential scan of Au QCM electrode in the electrolyte solution used for electrodeposition of $(Bi_2)_m(Bi_2Te_3)_n$

Fig. 3 Potentiodynamic cyclic voltammetry and microgravimetry of Au QCM electrode at 10 mV/s in (**a**, **b**) 7.5 mM Bi(NO$_3$)$_3$, 2.5 mM TeO$_2$, 1 M HNO$_3$, **c** 10 mM Bi(NO$_3$)$_3$ 1 M HNO$_3$, **d** 1 mM TeO$_2$, 1 M HNO$_3$; **b** shows the magnified fragment of **a**
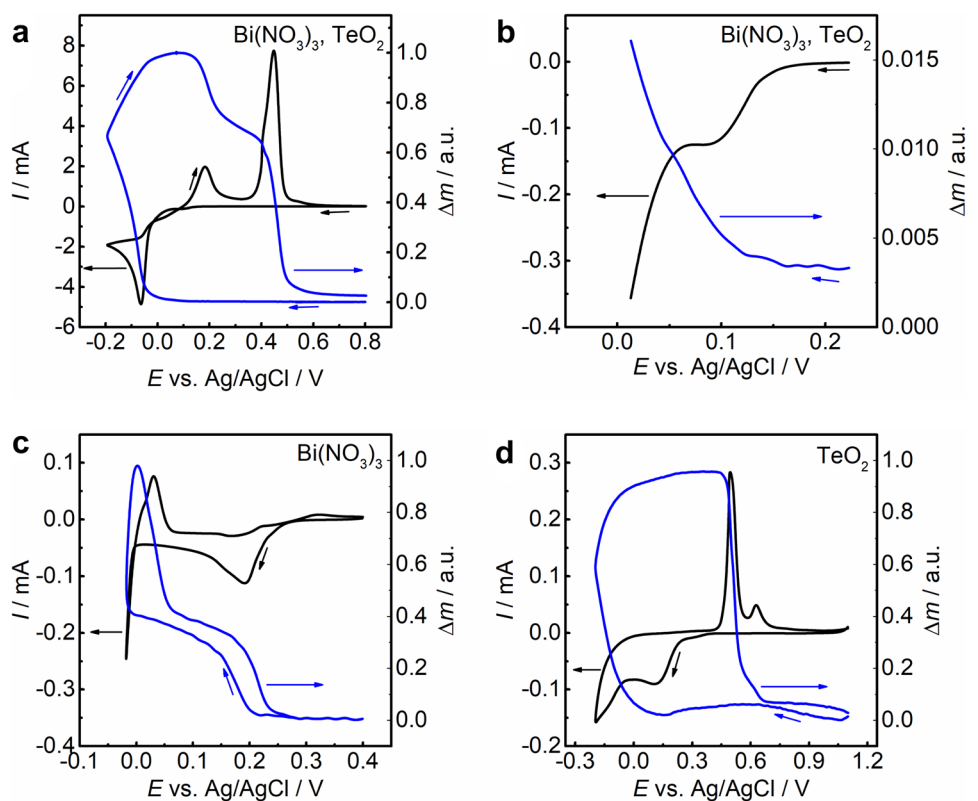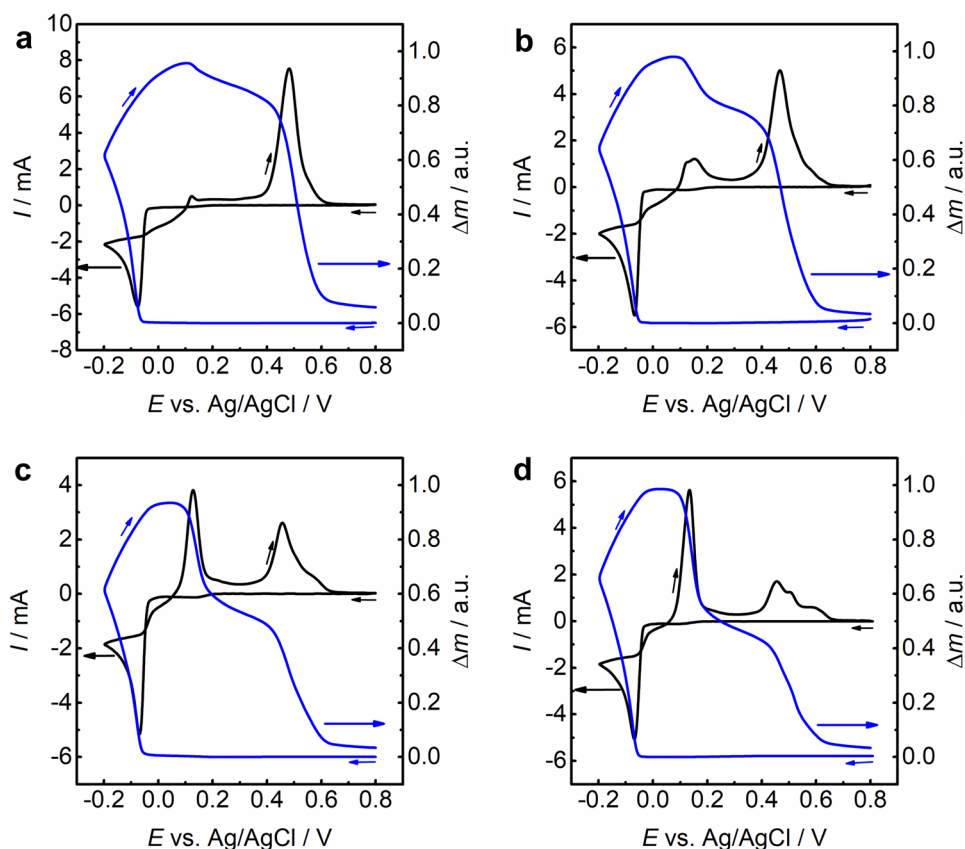
superlattices with bismuth bilayers at "low" bismuth content. Figure 3c, d present variations of the same parameters in the separate solutions of Bi(III) and Te(IV) precursors. The low cathodic current and small mass increase, which start at approx. 0.15 V vs. Ag/AgCl reference electrode in the negative scan attributed to Au surface cooperative modification by adlayers of Te and Bi. The initial small decrease of mass in the cathodic scan in TeO_2 solution close to 0.2 V (Fig. 3d) is due to the removal of oxygen from adsorbed TeO_2 (or $HTeO_2^+$) during the adsorbed Te(IV) precursor reduction. Underpotential deposition of Bi on gold proceeds in the same potential region (Fig. 3c). The potentials of Bi upd on Te [28] and Bi upd on bismuth telluride (shown further in this work) are just very slightly more negative, so the electrodeposition of bismuth telluride can proceed via the upd in the composite solution of Bi(III) and Te(IV). The resulting presence or absence of bismuth interlayers in bismuth telluride is dependent on relative rates of the competing cathodic reactions which are, in their turn, controlled by precursor concentrations and program of the potential variation. The cyclic scan with potential reversal at -0.2 V discloses two peaks of the anodic current accompanied by the two corresponding mass decreases (Fig. 3a) at 0.2 V (bismuth interlayers) and 0.45 V (bismuth telluride), which indicate synchronous oxidation and dissolution processes in both consecutive anodic reactions.

Figure 4 shows the emergence and growth of interlayer bismuth signal in potentiodynamic voltammetry and microgravimetry with Bi(III):Te(IV) molar ratio increase in the electrolyte solution. At the two highest Bi(III)/Te(IV), the anodic oxidation of bismuth interlayers dominates over bismuth telluride anodic oxidation. Also, the stripping voltammogram of the latter shows a multi-peak structure which evidently results from fragmentation of bismuth telluride framework that becomes unstable when interlayers larger than bilayers are removed. The superlattices with low Bi content do not show this feature, which complies with the superlattice framework preservation at bismuth interlayer anodic dissolution from superlattice with low bismuth content earlier [19] discovered with XRD data analysis.

Figure 5 shows mass variations and potentiodynamic voltammetric response in bismuth nitrate solution of $(Bi_2)_m(Bi_2Te_3)_n$ which was pulse deposited at different molar ratio of precursors $C_{Bi(III)}/C_{Te(IV)}$. The left column (Fig. 5a, c) corresponds to low Bi content, the right column (Fig. 5b, d) high Bi content. The potential of negative scan reversal to positive scan was more negative in the second row (Fig. 5c, d) to provide metallic bismuth cathodic nucleation in addition to upd in the cathodic scan. The positive potential scans were started from open circuit potential and reversed before the potential of bismuth telluride anodic oxidation. Bismuth upd in the slits created by selective anodic dissolution of

Fig. 4 Potentiodynamic cyclic voltammetry and microgravimetry of Au QCM electrode during $(Bi_2)_m(Bi_2Te_3)_n$ cathodic deposition and anodic oxidation at 10 mV/s in electrolyte solutions of different Bi(III)/Te(IV) molar ratio: **a** 6.67 mM $Bi(NO_3)_3$, 3.33 mM TeO_2, 1 M HNO_3; **b** 7.5 mM $Bi(NO_3)_3$, 2.5 mM TeO_2, 1 M HNO_3; **c** 8.33 mM $Bi(NO_3)_3$, 1.67 mM TeO_2, 1 M HNO_3; **d** 8.75 mM $Bi(NO_3)_3$, 1.25 mM TeO_2, 1 M HNO_3

bismuth interlayers (upper row of plots) and both the upd and the nucleation of metallic bismuth (lower row of plots) are presented by potential dependences of current and mass and could be compared for the superlattice structures with bismuth bilayers (left column) and with thicker interlayers (right column). Though the underpotentially deposited bismuth reintroduced less than 20% of the anodically dissolved interlayer bismuth, its amount was orders of magnitude higher than the amount of bismuth which was underpotentially deposited onto Bi_2Te_3 film of similar thickness for comparison, e.g., the difference was two orders for the samples with high initial interlayer bismuth content. On the contrary, we did not observe significant enhancement of metallic bismuth deposition by the electrochemically created slits. Evidently, Bi upd proceeded essentially in the slits formed by Bi interlayer anodic dissolution, but the width of the slits was insufficient for electrodeposition of bismuth metallic particles even in samples with thicker interlayers. The lower row of plots also shows the discrimination by potentials of anodic oxidation of metallic Bi (anodic peak starting close to 0 V) and Bi of the interlayers (the anodic peak above 0.2 V in the first positive scan). Actually, this significant difference of oxidation potentials provided a reliable protection of $(Bi_2)_m(Bi_2Te_3)_n$ pulsed electrodeposition from effects of bismuth nucleation, as the greater time slot in $(Bi_2)_m(Bi_2Te_3)_n$ pulsed electrodeposition procedure is

allocated to the refinement stage at a potential of metallic bismuth anodic oxidation [19, 29]. The typical potential of $(Bi_2)_m(Bi_2Te_3)_n$ electrodeposition stage — -100 mV [29] — was sufficient for Bi nucleation, but the periodic switching of the potential upward into the region where metallic bismuth was oxidized with preservation of Bi bilayers, and adatoms helped to keep the smooth growth of the layered structure in the pulse potential–controlled deposition.

Potentiodynamic electrochemical impedance spectroscopy

The anodic oxidation of bismuth interlayers is dependent on evacuation rate of the reaction product Bi(III) (Bi^{3+} cations with anions attached to them in the solution for charge compensation), as follows from the effect of electrolyte shown in Fig. 2. The potentiodynamic microgravimetry has disclosed the synchronous electrode mass decrease and charge transfer in the anodic oxidation. The further separate characterization of the charge transfer, diffusion, and double layer charging is the field of impedance spectroscopy. Impedance spectroscopy is especially helpful in combination with QCM and other in situ electrochemical techniques [30–32].

Inherent non-stationarity of the anodic dissolution of bismuth from interlayers in bismuth–bismuth telluride superlattices, as well as the non-stationarity of subsequent bismuth

Fig. 5 Potentiodynamic cyclic voltammetry and microgravimetry of $(Bi_2)_m(Bi_2Te_3)_n$ film electrodes pulse deposited from **a, c** 7.5 mM $Bi(NO_3)_3$, 2.5 mM TeO_2, 1 M HNO_3, **b, d** 8.33 mM $Bi(NO_3)_3$, 1.67 mM TeO_2, 1 M HNO_3. Electrolyte: 10 mM $Bi(NO_3)_3$, 1 M HNO_3, $dE/dt = 1$ mV s^{-1}. In **a** and **b**, the negative scan was reversed immediately after Bi upd into anodically created slits; **c** and **d** additionally show cathodic deposition and anodic oxidation of metallic bismuth
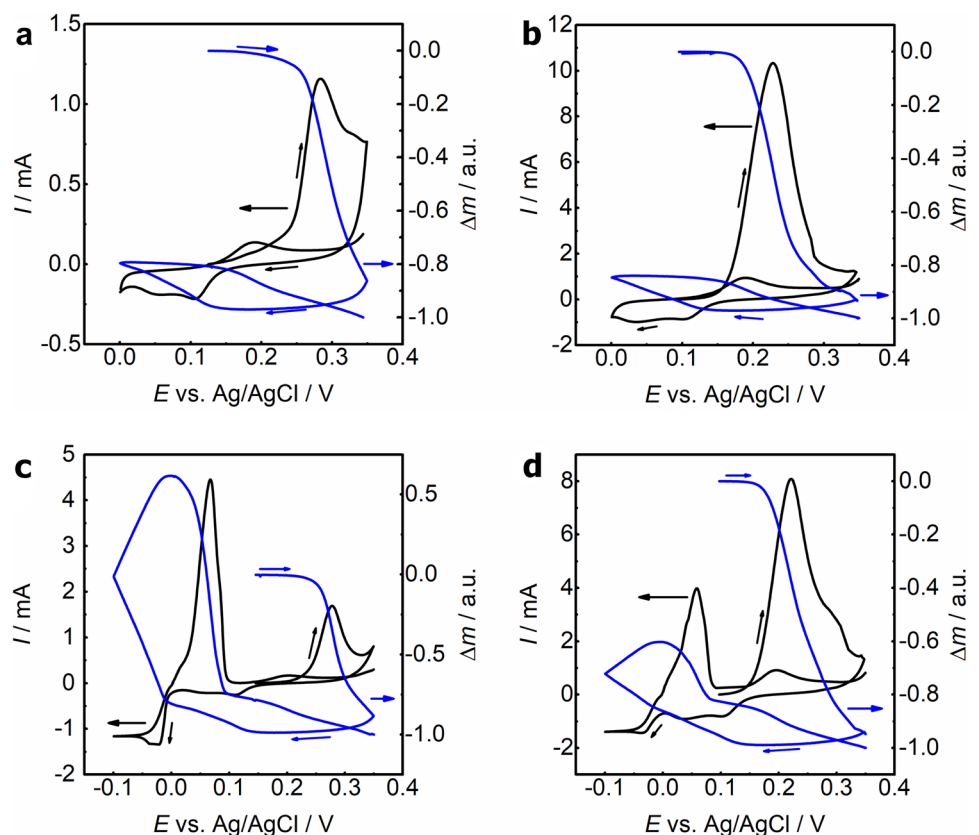
underpotential deposition into the electrochemically created slits, presents a critical hindrance to application of stationary impedance spectroscopy for examination of these processes. This kind of objects is appropriate for examination with non-stationary EIS [33, 34].

Figure 6 shows a typical PDEIS spectrum of bismuth–bismuth telluride superlattice with bismuth content sufficiently low to accommodate all the excessive bismuth in bilayers between bismuth telluride quintuples. The spectrum presents the frequency response variation during the selective anodic oxidation of bismuth interlayers in the positive potential scan. The impedance spectrum is shown as a 3D surface formed by translation of Nyquist plot along the potential axis at 0.9 mV s^{-1} scan rate in the direction perpendicular to the plane formed by Z(im) and Z(re) axes. The snapshots of frequency response are acquired in PDEIS at fixed potentials; however, fast algorithms of the frequency response acquisition and the use of very small steps along the potential axis (2 mV in this case) provide a quasi-continuous recording of the impedance spectrum and a dc voltammogram; the dc and frequency responses are simultaneously recorded in a way similar to that in staircase voltammetry with small but discrete increments of the potential in a quasi-linear potential scan. The potentiodynamic voltammogram is presented on the invisible front plane of the parallelepiped formed by Z(im), Z(re), and E axes (the parallelepiped edge opposite to Z(im) shows values of the current in the voltammogram). The three planes of the parallelepiped closest to observer were made invisible to facilitate observation of the 3D spectrum inside the parallelepiped.

Similarly to potentiodynamic voltammetry which graphically presents dynamics of electrochemical reactions, PDEIS also shows the dynamic electrochemical response already in the time of the potential scan, and the potentiodynamic frequency response discloses some peculiarities hidden from revelation both by stationary EIS and potentiodynamic voltammetry even before analysis of the frequency response in terms of equivalent circuits, e.g., the PDEIS spectrum in Fig. 6a discloses graphically a high capacitive response at the potential of voltammetric peak by the imaginary impedance hollow (the direction of the potential scan is indicated in Fig. 6a with a sequence of small green arrows at the lowest frequency; Fig. 6b shows the imaginary impedance variation by the orthogonal projection of the same spectrum). The further quantitative analysis in terms of equivalent electric circuits by method and software described in [22] confirms the visual information by potentiodynamic profiles of the respective capacitances.

The best fit equivalent circuit in the potential region of Bi interlayer anodic oxidation (Fig. 6c) contains two capacitances, the double-layer capacitance C_{dl} and the capacitance C_p in the faradaic branch in parallel with C_{dl}. Impedance of diffusion has shown some variable spatial confinement which resulted in its accurate fitting to finite-length diffusion with transmissive boundary circuit element Z_{Ws}, similar to the one that represents diffusion impedance in impedance spectroscopy on rotating disc electrode (Warburg Short element [35]). The presence of the finite-length Warburg element in the equivalent circuits
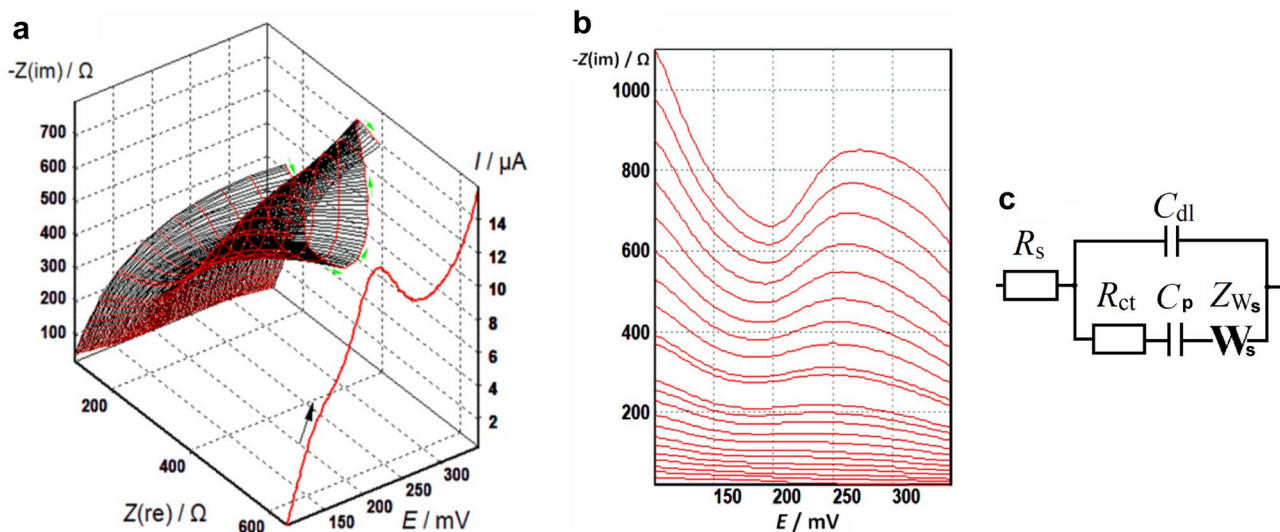

Fig. 6 **a** PDEIS 3D spectrum recorded during Bi selective anodic dissolution from $(Bi_2)m(Bi_2Te_3)_n$ at 0.9 mV s^{-1}, **b** the orthogonal projection of the same 3D spectrum showing imaginary impedance variation in the potential scan (frequency increases from top to bottom in the series of red lines), and **c** the best fit equivalent electric circuit

evidently results from spatially confined diffusion profiles of the mass transport from and to the slits in superlattice which required the use of two parameters of diffusion impedance instead of single Warburg coefficient A_W of semi-infinite diffusion. The second parameter, A_{W1}, in Warburg short accounts for spatial restriction imposed on mass transport.

The capacitance C_p results from availability of bidirectional electron transfer in one or more steps of the irreversible as a whole three-electron redox reaction

$$Bi \rightarrow Bi^{3+} + 3e^- \tag{1}$$

The entire reaction lacks reversibility both in the anodic bismuth interlayer dissolution and in Bi upd in the anodically formed cavities. The irreversibility of the former reaction follows from incomplete filling of the cavities by bismuth cathodic deposition (shown in the previous section with QCM). The electrochemical irreversibility of Bi upd follows from the separation on the potential of the

non-overlapping cathodic and anodic currents of Bi upd and anodic oxidation of Bi adatoms (Fig. 5). The irreversibility originates from evacuation of the reaction product, which is a slow process, while on a short time scale, the charge transfer in reaction (1) is reversible, similarly to the charge transfer in the earlier [21, 36] examined reaction (1) in Bi upd on gold. Reversibility of charge transfer in upd manifests itself by adsorption capacitance in the Faradaic branch of equivalent electric circuit [34, 36]. The corresponding circuit element C_p was clearly disclosed in the anodic bismuth interlayer dissolution by PDEIS data analysis.

The capacitance C_p is much higher than the double-layer capacitance (Fig. 7a, b), and this is typical to adsorption capacitances that result from fast bidirectional electron transfer in surface-restricted electrochemical reactions [37–39]. Unlike C_{dl}, which gradually rises, due to the electrochemically active interface proliferation during the anodic oxidation and dissolution of bismuth from
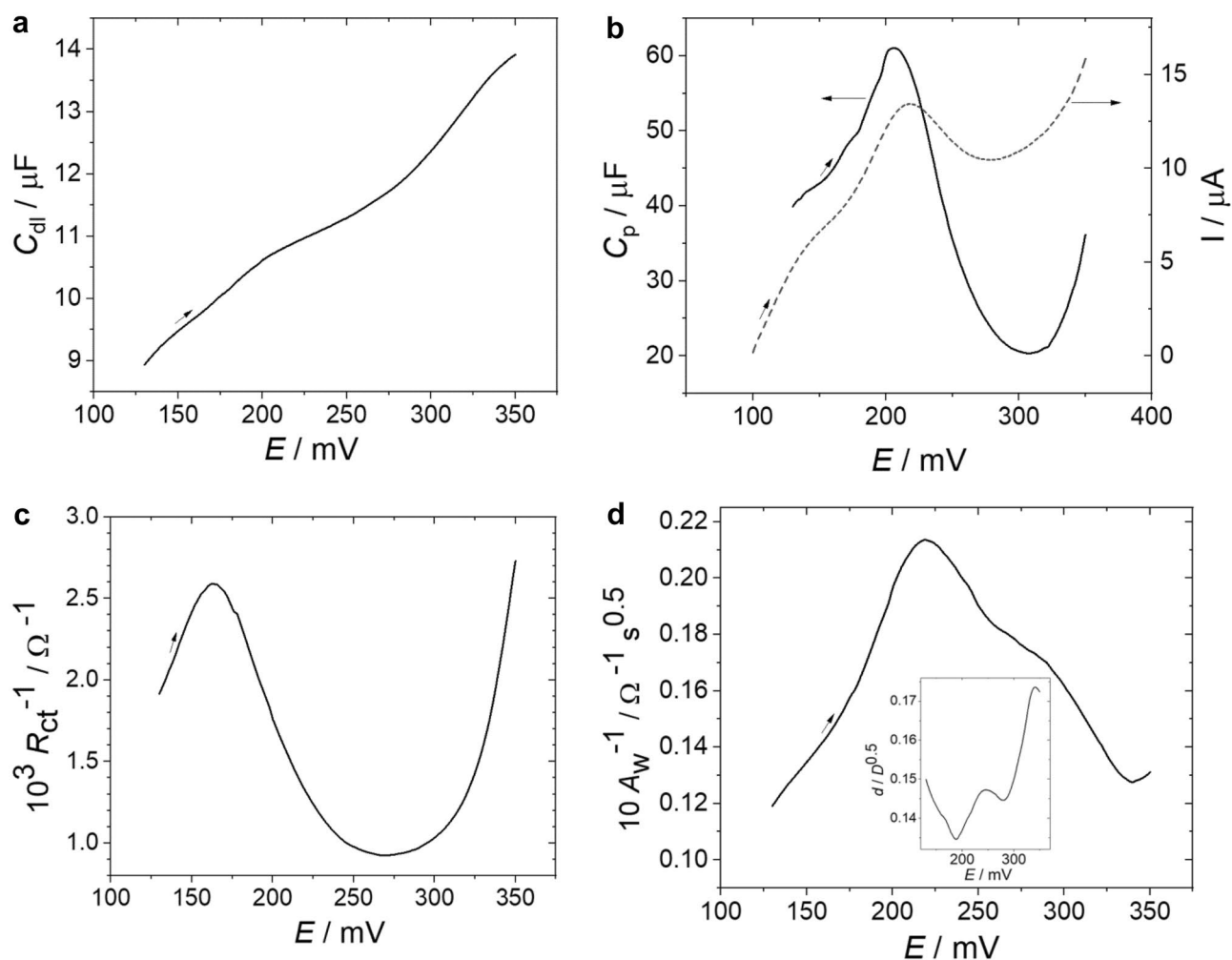

Fig. 7 Potentiodynamic profiles of PDEIS parameters **a** C_{dl}, **b** C_p, **c** R_{ct}, **d** A_W, and A_{W1} (inset in **d**) corresponding to Fig. 6
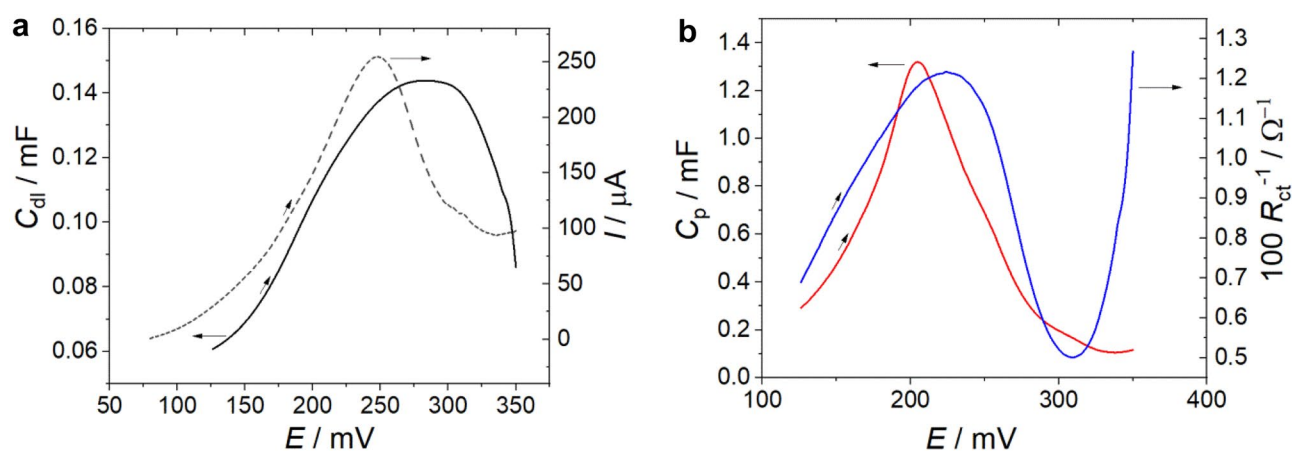
Fig. 8 PDEIS parameters of the model shown in Fig. 6c at Bi anodic oxidation from $(Bi_2)_m(Bi_2Te_3)_n$ at high Bi content; **a** C_{dl} and current I, **b** C_p and R_{ct}

the interlayers, C_p shows maximum value shortly before the voltammetric peak. This complies with C_p attribution to the surface confined redox reaction. The maxima of inverse values of charge transfer resistance R_{ct}^{-1} (Fig. 7c) and Warburg coefficient A_W^{-1} (Fig. 7d) are shifted in the opposite directions from the voltammetric peak. The R_{ct}^{-1} peak tends to a reversible potential of a redox reaction which should correspond to some point on the rising part of the anodic voltammogram (specifically, the point of intercept of $R_{ct}^{-1}(E)$ plots for forward and back reactions [28]), while a significant positive shift of A_W^{-1} peak indicates some variation of the diffusion conditions during the anodic dissolution of bismuth from interlayers. The variation of mass transport conditions is further confirmed by the complex dependence of the spatial parameter of diffusion impedance A_{W1} shown in inset to Fig. 7d, but at this stage of investigation, we are not yet prone to attribute any physical meaning to maxima and minima in $A_{W1}(E)$ plots which appeared to be rather variable at variable conditions of experiment. Due to random distribution of bismuth interlayers between stacks of Bi_2Te_3 quintuples in $(Bi_2)_m(Bi_2Te_3)_n$ superlattices of variable composition, the model should have probably contained more than a single parameter related to the superlattice structure effect on diffusion; A_{W1}^{-1} probably just averages effects of several parameters, thus allowing accurate derivation of other parameters of the circuit. The use of "Warburg short" instead of ordinary Warburg element in the analysis of this system frequency response variation is somewhat analogous to the use of constant phase element for representation of distorted double-layer capacitances, i.e., the additional parameter is required for providing high quality of derivation of other parameters though the physical meaning of the additional parameter itself may be not always clear. However, in system with a single diffusion length restriction, e.g., in potentiodynamic electrochemical

impedance spectroscopy on rotating disc electrode, A_{W1} is very informative as it is equal to diffusion length d ratio to square root of diffusion coefficient D, $A_{W1} = d/D^{0.5}$ [40].

The net formula for the superlattice with maximum number of bismuth bilayers is Bi_4Te_3, which corresponds to the condition $m = n$ in $(Bi_2)_m(Bi_2Te_3)_n$. With further increase in bismuth content, we observed the transformation of the gradually rising $C_{dl}(E)$ of the kind shown in Fig. 7a to a plot with C_{dl} maximum in the range of the interlayer bismuth anodic oxidation (Fig. 8a). At high bismuth content, the superlattice cannot accommodate all the excessive bismuth in bilayers, so the excessive bismuth forms thicker interlayers, such as Bi_4 in Bi_2Te, and the anodic destruction of the thick interlayers appears to be more harmful to the superlattice which shrinks according to our earlier XRD examination [19]. The abrupt decrease in C_{dl} which was observed above the potential of the voltammetric peak or even earlier in the anodic scan, depending on $(Bi_2)_m(Bi_2Te_3)_n$ composition, evidently manifests this shrinkage of the Bi_2Te_3 framework during the anodic dissolution of bismuth interlayers. Both capacitances (Fig. 8a, b) were much higher at high Bi content, indicating higher electroactive surface area. Also, the relative increase of the capacitances before they started to fall was higher than in the case shown in Fig. 7, which indicated a greater electrochemical accessibility of the anodically proliferated interface in structures with originally high Bi content. Similarly to the case of low Bi content, $R_{ct}^{-1}(E)$ showed maximum corresponding to Bi anodic oxidation and started to rise again above 300 mV thus indicating the start of Bi_2Te_3 framework anodic oxidation. Shortly above this potential, the frequency response usually became unstable, which prevented from its analysis at higher potential.

The electrochemical mobility of bismuth in the interlayers is of interest for further design of complex

thermoelectric materials by replacing bismuth by atoms of other elements with preservation of bismuth telluride framework. The electrochemical introduction of atoms of other elements, such as zinc [41], into layered structure of metal chalcogenides is also of interest for development of advanced aqueous batteries.

Raman spectroscopy

In situ Raman spectroscopy combined with cyclic voltammetry provides additional information about $(Bi_2)_m(Bi_2Te_3)_n$ superlattice transformations during selective anodic oxidation of bismuth interlayers, subsequent electrodeposition and anodic oxidation of Bi adatoms and metallic bismuth. The spectra were continuously recorded in the potentiodynamic mode; the data acquisition of each spectrum took 30 s, which corresponded to 30 mV in the potential scan.

To analyze the data obtained from in situ Raman experiment, we consider the four states of the superlattice variation during the experiment indicated by Roman numerals in the voltammograms (Fig. 9a, d). The state I corresponds to the superlattice at the beginning of the experiment at OCP. The state II is achieved by the selective anodic oxidation of bismuth interlayers. After the potential scan reversal, the selectively oxidized superlattice acquires Bi adatoms in two stages of Bi upd (upd 1 and upd 2) distinguished both in CV

and in situ Raman and thus enters the state III. The next state IV is obtained during the subsequent deposition of metallic bismuth. Then, as a result of metallic bismuth anodic oxidation, the object reaches the state analogous to state III (state III') which has no metallic Bi but still contains Bi adatoms. After the anodic oxidation of Bi adatoms, we obtain the state II again.

Figure 9b, e show full spectral maps for two potential cycles on the superlattices with originally low (Fig. 9b) and high (Fig. 9e) Bi content. Due to different effect of Au (in QCM experiment) and steel (in Raman) substrates on kinetics of $(Bi_2)_m(Bi_2Te_3)_n$ pulsed electrodeposition, the sample with low Bi content contained less Bi in the latter case than in QCM experiment, and this difference was kept to provide convenient simultaneous spectral characterization of both the interlayered Bi and Bi adatoms which were cathodically introduced into the superlattice after the anodic oxidation of Bi interlayers. The start of the spectral map is at the bottom of the ordinate axis at the potential that corresponds to the open circuit potential of $(Bi_2)_m(Bi_2Te_3)_m$ of the given composition in 10 mM $Bi(NO_3)_3$, 1 M HNO_3 electrolyte (0.11 V for the superlattice with low bismuth content and 0.07 V for the superlattice with high bismuth content).

Figure 9b, e show that the key feature in the transitions between states I and II during the selective oxidation of the interlayered bismuth consists in the great increase in the
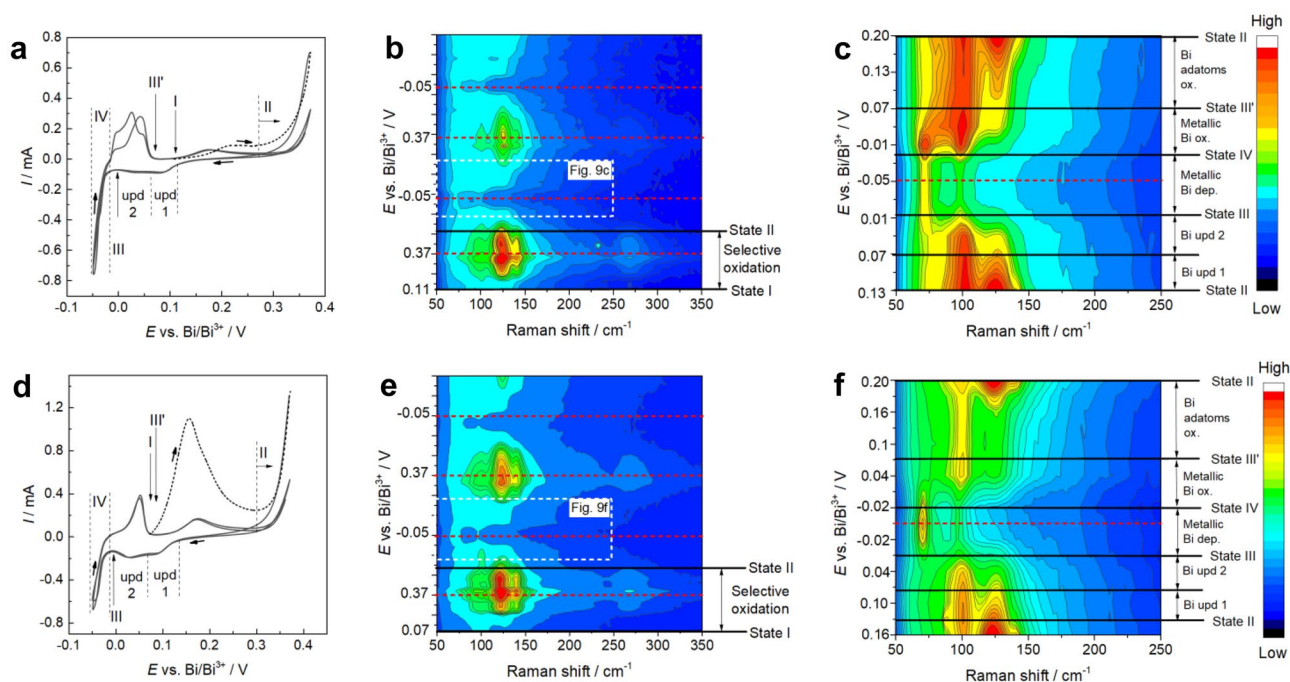

Fig. 9 **a**, **d** Potentiodynamic cyclic voltammograms and **b**, **c**, **e**, **f** in situ Raman spectra potentiodynamic maps of pulse deposited $(Bi_2)_m(Bi_2Te_3)_n$ films with low (**a–c**) and high (**d–f**) interlayer Bi content in cyclic potential scans at 1 mV s^{-1} starting from open circuit potential in 10 mM $Bi(NO_3)_3$, 1 M HNO_3 electrolyte solution (the starting potentiodynamic profiles are shown in **a**, **d** by dotted lines). Red lines in the spectral maps show the potentials of the scan direction reversal, black lines — boundaries in the transitions between the states indicated by Roman numerals in the voltammograms (**a**, **d**)

Raman intensity of the E^2_g mode at 101 cm^{-1} and A^2_{1g} mode at 125 cm^{-1} inherent to bismuth telluride [42]. Moreover, there is intensity redistribution in favor of the A^2_{1g} mode, which could be explained taking into account participation of bismuth electrons in formation of the E^2_g mode of bismuth telluride. The observed shifts in characteristic frequencies at early stages of the oxidation can be attributed to the change in the predominant interaction between the building blocks, as Coulomb interaction between bismuth telluride quintuples and Bi is reduced with Bi anodic oxidation and dissolution [43]. The dramatic increase in the Raman signal intensity shown by appearance of brown areas in the maps can result from exposure of tellurium-terminated facets that have larger cross-sectional area for Raman scattering [44, 45], when bismuth of interlayers leaves the superlattice.

The parts of Fig. 9b, e outlined with white dotted rectangles are shown in the magnified form in Fig. 9c, f for detailed representation of changes in spectral map during the deposition of Bi adatoms and metallic Bi, as well as their subsequent anodic oxidation. The cyclic voltammetry shows the double-peak structure of Bi upd voltammetric response. We did not observe any corresponding internal differentiation in the upd with QCM, but the Raman spectroscopy shows that the first stage of Bi upd causes a decrease in Raman intensity of the mode at 125 cm^{-1}, whereas the second stage leads to a decrease in the intensity of the mode at 101 cm^{-1}. It is worth to mention that the spectrum recorded after the second step of the Bi upd resembled the spectrum of the initial superlattice in state I. We assume that in the first stage of Bi upd, adatoms interact only with tellurium-terminated facets, and this interaction reduces the intensive Raman signal grown during the selective oxidation of bismuth interlayers. In the second stage, adatoms interact with each other, partially regenerating bilayer structure and thus causing the spectrum appearance close to the one of the initial superlattice.

The deposition of metallic bismuth during the transition from the state III to the state IV suppresses the mode at 101 cm^{-1} and gives rise to the E_g bismuth mode at 71 cm^{-1}. This change in Raman spectrum in combination with our QCM and CV data allows to distinguish reliably metallic bismuth from bismuth of interlayers in $(Bi_2)_m(Bi_2Te_3)_m$ superlattices, contrary to assignment of bismuth with enhanced anodic oxidation potential to free bismuth in some works on bismuth telluride electrodeposition [46]. Bismuth of the interlayers shows more similarity with adatoms than with metallic bismuth.

The oxidation of metallic bismuth during the transition from the state IV to III′ returns the mode at 101 cm^{-1}, and the following oxidation of Bi adatoms that finishes at about 0.2 V regenerates state II with the Raman intensity increase at 125 cm^{-1} revealing the re-exposure of tellurium-terminated facets. Moreover, this shows that both the deposition of Bi

adatoms and metallic bismuth into and onto the superlattice distorted by oxidation of bismuth interlayers proceeds reversibly, i.e., with regeneration of similar states in the potential cycles, which is also in compliance with the cyclic character of transformations observed in QCM experiments.

Conclusion

The four methods were applied in the potentiodynamic mode for in situ characterization of bismuth interlayer selective anodic oxidation and dissolution from $(Bi_2)_m(Bi_2Te_3)_n$ superlattice: cyclic voltammetry, microgravimetry, potentiodynamic electrochemical impedance spectroscopy, and in situ Raman spectroscopy. The cyclic voltammetry in a combination with microgravimetry provided monitoring of bismuth removal from interlayers during the selective anodic oxidation and the subsequent reverse mass transfer during Bi upd in the electrochemically formed slits. The potentiodynamic electrochemical impedance spectroscopy has differentiated the electrochemical response by contributions of the interfacial charge transfer related to the electrochemical kinetics, the charging of double layer capacitance, and the capacitance of faradaic origin, and also provided detailed information on mass transport. The latter has shown spatial restrictions originated in the superlattice structure. The potentiodynamic profiles of double-layer capacitance have disclosed different variations of the electrochemical interface area in the anodic dissolution of interlayer bismuth from superlattices with low and high bismuth content. The continuously growing interface of the former complies with the stability of the corresponding naked superlattice framework, while the abrupt C_{dl} decrease after initial growth in the anodic dissolution of bismuth from superlattice with high bismuth content indicates the telluride network shrinkage resulting from removal of bismuth from thicker interlayers. With the further addition of in situ Raman spectroscopy, we obtained information on localization of bismuth adatoms which were deposited into the slits formed by selective bismuth anodic dissolution from the interlayers. The double-peak structure of Bi upd observed with cyclic voltammetry was shown to result from the electrodeposition of adatoms at potentials of the first peak followed by the adatoms joining up into fragments of the previously destroyed interlayer.

Thus, bismuth interlayers in $(Bi_2)_m(Bi_2Te_3)_n$ superlattices present a very interesting object to electrochemistry. Their potential of anodic oxidation is intermediate between the potentials of anodic oxidation of metallic bismuth and bismuth telluride, and this provided both the efficient control of electrodeposition of the superlattices and the further selective dissolution of bismuth from the superlattices. The proliferation of $(Bi_2)_m(Bi_2Te_3)_n$ electrode interface during the selective anodic oxidation and dissolution of bismuth

from interlayers presents the opportunity to create slits accessible for Bi^{3+} penetration from electrolyte solution with subsequent formation of unusually high amount of Bi adatoms by upd. In principle, the slits formed by interlayer dissolution can also act as molecular sieve that allows penetration of molecules of certain size corresponding to bismuth bilayer or quadruple thickness, which is a potentially interesting means to control selective accessibility of dissolved substance to catalytic centers formed inside the slits by upd, in addition to the main interest of material science in $(Bi_2)_m(Bi_2Te_3)_n$ as thermoelectric material and a precursor of other thermoelectric materials which can be designed via the electrochemical transformations of the interlayers.

References

1. Bos JWG, Zandbergen HW, Lee MH et al (2007) Structures and thermoelectric properties of the infinitely adaptive series $(Bi_2)_m(Bi_2Te_3)_n$. Phys Rev B - Condens Matter Mater Phys 75:195203. https://doi.org/10.1103/PhysRevB.75.195203

2. Sharma PA, Lima-Sharma AL, Medlin DL et al (2011) Low phonon thermal conductivity of layered $(Bi_2)_m$-$(Bi_2Te_3)_n$ thermoelectric alloys. Phys Rev B - Condens Matter Mater Phys 83:235209. https://doi.org/10.1103/PhysRevB.83.235209

3. Zhu H, Zhao C, Nan P et al (2021) Intrinsically low lattice thermal conductivity in natural superlattice $(Bi_2)_m(Bi_2Te_3)_n$ thermoelectric materials. Chem Mater 33:1140–1148. https://doi.org/10.1021/acs.chemmater.0c03691

4. Zhou J, Jin C, Seol JH et al (2005) Thermoelectric properties of individual electrodeposited bismuth telluride nanowires. Appl Phys Lett 87:133109. https://doi.org/10.1063/1.2058217

5. Marcilla R, Ochoteco E, Pomposo JA, Mecerreyes D (2001) Electrodeposition of ordered Bi_2Te_3 nanowires array. J Am Chem Soc 123:7160–7161. https://doi.org/10.1021/ja015989j

6. Menke EJ, Li Q, Penner RM (2004) Bismuth telluride (Bi_2Te_3) nanowires synthesized by cyclic electrodeposition / stripping coupled with step edge decoration. Nano Lett 4:2009–2014. https://doi.org/10.1021/nl048627t

7. Lee J, Farhangfar S, Lee J et al (2008) Tuning the crystallinity of thermoelectric Bi_2Te_3 nanowire arrays grown by pulsed electrodeposition. Nanotechnology 19:365701. https://doi.org/10.1088/0957-4484/19/36/365701

8. Mavrokefalos A, Moore AL, Pettes MT et al (2009) Thermoelectric and structural characterizations of individual electrodeposited bismuth telluride nanowires. J Appl Phys 105:104318. https://doi.org/10.1063/1.3133145

9. Bejenari I, Kantser V, Balandin AA (2010) Thermoelectric properties of electrically gated bismuth telluride nanowires. Phys Rev B - Condens Matter Mater Phys 81:075316. https://doi.org/10.1103/PhysRevB.81.075316

10. Frantz C, Stein N, Gravier L et al (2010) Electrodeposition and characterization of bismuth telluride nanowires. J Electron Mater 39:2043–2048. https://doi.org/10.1007/s11664-009-1001-2

11. Borca-Tasciuc DA, Chen G, Prieto A et al (2004) Thermal properties of electrodeposited bismuth telluride nanowires embedded in amorphous alumina. Appl Phys Lett 85:6001–6003. https://doi.org/10.1063/1.1834991

12. Chang T, Cho S, Kim J et al (2015) Individual thermoelectric properties of electrodeposited bismuth telluride nanowires in polycarbonate membranes. Electrochim Acta 161:403–407. https://doi.org/10.1016/j.electacta.2015.02.105

13. Chatterjee K, Suresh A, Ganguly S et al (2009) Synthesis and characterization of an electro-deposited polyaniline-bismuth telluride nanocomposite - a novel thermoelectric material. Mater Charact 60:1597–1601. https://doi.org/10.1016/j.matchar.2009.09.012

14. Lind H, Lidin S, Häussermann U (2005) Structure and bonding properties of $(Bi_2Se_3)_m(Bi_2)_n$ stacks by first-principles density functional theory. Phys Rev B - Condens Matter Mater Phys 72:184101. https://doi.org/10.1103/PhysRevB.72.184101

15. Gibson QD, Schoop LM, Weber AP et al (2013) Termination-dependent topological surface states of the natural superlattice phase Bi_4Se_3. Phys Rev B - Condens Matter Mater Phys 88:081108. https://doi.org/10.1103/PhysRevB.88.081108

16. Valla T, Ji H, Schoop LM et al (2012) Topological semimetal in a Bi-Bi_2Se_3 infinitely adaptive superlattice phase. Phys Rev B - Condens Matter Mater Phys 86:241101. https://doi.org/10.1103/PhysRevB.86.241101

17. Samanta M, Biswas K (2020) 2D nanosheets of topological quantum materials from homologous $(Bi_2)_m(Bi_2Se_3)_n$ heterostructures: Synthesis and ultralow thermal conductivity. Chem Mater 32:8819–8826. https://doi.org/10.1021/acs.chemmater.0c02129

18. Johannsen JC, Autès G, Crepaldi A et al (2015) Engineering the topological surface states in the $(Sb_2)_m$-Sb_2Te_3 (m=0-3) superlattice series. Phys Rev B - Condens Matter Mater Phys 91:201101. https://doi.org/10.1103/PhysRevB.91.201101

19. Bakavets A, Aniskevich Y, Yakimenko O et al (2020) Pulse electrodeposited bismuth-tellurium superlattices with controllable bismuth content. J Power Sources 450:227605. https://doi.org/10.1016/j.jpowsour.2019.227605

20. Ragoisha GA, Bondarenko AS (2003) Potentiodynamic electrochemical impedance spectroscopy for solid state chemistry. Solid State Phenom 90–91:103–108. https://doi.org/10.4028/www.scientific.net/SSP.90-91.103

21. Ragoisha GA, Bondarenko AS (2005) Potentiodynamic electrochemical impedance spectroscopy. Electrochim Acta 50:1553–1563. https://doi.org/10.1016/j.electacta.2004.10.055

22. Bondarenko AS, Ragoisha GA (2005) Inverse problem in potentiodynamic electrochemical impedance. In: Progress in Chemometrics Research. Nova Science Publ, New York, pp 89–102. http://www.novapublishers.org/catalog/product_info.php?products_id=2337

23. Bondarenko AS, Ragoisha GA (2008) EIS Spectrum Analyser. http://www.abc.chemistry.bsu.by/vi/analyser/

24. Inzelt G, Kertész V, Nybäck AS (1999) Electrochemical quartz crystal microbalance study of ion transport accompanying charging-discharging of poly(pyrrole) films. J Solid State Electrochem 3:251–257. https://doi.org/10.1007/s100080050155

25. Inzelt G (1990) A quartz crystal microbalance study of the sorption of ions and solvent molecules in poly(tetracyanoquinodimethane) electrodes. J Electroanal Chem Interf Electrochem 287:171–177. https://doi.org/10.1016/0022-0728(90)87167-I

26. Inzelt G, Berkes B, Kriston Á (2010) Temperature dependence of two types of dissolution of platinum in acid media. An electrochemical nanogravimetric study Electrochim Acta 55:4742–4749. https://doi.org/10.1016/j.electacta.2010.03.074

27. Buck RP, Lindner E, Kutner W, Inzelt G (2004) Piezoelectric chemical sensors (IUPAC technical report). Pure Appl Chem 76:1139–1160. https://doi.org/10.1351/pac200476061139

28. Chulkin PV, Aniskevich YM, Streltsov EA, Ragoisha GA (2015) Underpotential shift in electrodeposition of metal adlayer on

tellurium and the free energy of metal telluride formation. J Solid State Electrochem 19:2511–2516. https://doi.org/10.1007/s10008-015-2831-x

29. Bakavets A, Aniskevich Y, Ragoisha G et al (2021) The optimized electrochemical deposition of bismuth-bismuth telluride layered crystal structures. IOP Conf Ser Mater Sci Eng 1140:012016. https://doi.org/10.1088/1757-899x/1140/1/012016

30. Inzelt G (1995) Characterization of modified electrodes by electrochemical quartz crystal microbalance, radiotracer technique and impedance spectroscopy. Electroanalysis 7:895–903. https://doi.org/10.1002/elan.1140070918

31. Inzelt G, Láng G (1991) Impedance analysis of poly (tetracyanoquinodimethane) electrodes: effect of electrolyte concentration and temperature. Electrochim Acta 36:1355–1361. https://doi.org/10.1016/0013-4686(91)80016-2

32. Inzelt G, Láng GG (2010) Electrochemical impedance spectroscopy (EIS) for polymer characterization. In: Electropolymerization: Concept Mater App, Wiley pp 51–76. https://doi.org/10.1002/9783527630592.ch3

33. Ragoisha GA (2020) Challenge for electrochemical impedance spectroscopy in the dynamic world. J Solid State Electrochem 24:2171–2172. https://doi.org/10.1007/s10008-020-04679-y

34. Ragoisha GA, Aniskevich YM, Bakavets AS, Streltsov EA (2020) Electrochemistry of metal adlayers on metal chalcogenides. J Solid State Electrochem 24:2585–2594. https://doi.org/10.1007/s10008-020-04681-4

35. Bondarenko AS, Ragoisha GA (2008) EIS Spectrum Analyser online manual. http://www.abc.chemistry.bsu.by/vi/analyser/parameters.html

36. Ragoisha GA (2015) Potentiodynamic electrochemical impedance spectroscopy for underpotential deposition processes. Electroanalysis 27:855–863. https://doi.org/10.1002/elan.201400648

37. Bondarenko AS, Ragoisha GA, Osipovich NP, Streltsov EA (2005) Potentiodynamic electrochemical impedance spectroscopy of lead upd on polycrystalline gold and on selenium atomic underlayer. Electrochem Commun 7:631–636. https://doi.org/10.1016/J.ELECOM.2005.04.001

38. Conway BE, Barber J, Morin S (1998) Comparative evaluation of surface structure specificity of kinetics of UPD and OPD of H at single-crystal Pt electrodes. Electrochim Acta 44:1109–1125. https://doi.org/10.1016/S0013-4686(98)00214-X

39. Ragoisha GA, Bondarenko AS (2003) Potentiodynamic electrochemical impedance spectroscopy. Copper underpotential deposition on gold. Electrochem Commun 5:392–395. https://doi.org/10.1016/S1388-2481(03)00075-4

40. Chulkin PV, Ragoisha GA (2010) Impedance spectroscopy on rotating disc electrode. Sviridov Readings, BSU 6:132–140 (in Russian)

41. Peng L, Ren X, Liang Z et al (2021) Reversible proton co-intercalation boosting zinc-ion adsorption and migration abilities in bismuth selenide nanoplates for advanced aqueous batteries. Energy Storage Materials 42:34–41. https://doi.org/10.1016/j.ensm.2021.07.015

42. Richter W, Kohler H, Becker CR (1977) A Raman and far-infrared investigation of phonons in the rhombohedral V_2–VI_3 compounds Bi_2Te_3, Bi_2Se_3, Sb_2Te_3 and $Bi_2(Te_{1-x}Se_x)_3$ $(0 < x < 1)$, $(Bi_{1-y}Sb_y)_2Te_3$ $(0 < y < 1)$. Phys Stat Sol B 84:619–628. https://doi.org/10.1002/pssb.2220840226

43. Zhang J, Huang G (2014) Phonon dynamics in $(Bi_2Se_3)_m(Bi_2)_n$ infinitely adaptive series. Solid State Commun 197:34–39. https://doi.org/10.1016/j.ssc.2014.08.004

44. Russo V, Bailini A, Zamboni M et al (2008) Raman spectroscopy of Bi-Te thin films. J Raman Spectrosc 39:205–210. https://doi.org/10.1002/jrs.1874

45. Rodríguez-Fernández C, Manzano CV, Romero AH et al (2016) The fingerprint of Te-rich and stoichiometric Bi_2Te_3 nanowires by Raman spectroscopy. Nanotechnology 27:075706. https://doi.org/10.1088/0957-4484/27/7/075706

46. Ham S, Jeon S, Lee U et al (2008) Compositional analysis of electrodeposited bismuth telluride thermoelectric thin films using combined electrochemical quartz crystal microgravimetry-stripping voltammetry. Anal Chem 80:6724–6730. https://doi.org/10.1021/ac8008127